

# Satellite-based assessment of rainfall-triggered landslide hazard for situational awareness

Dalia Kirschbaum<sup>1</sup>, Thomas Stanley<sup>2,1</sup>

<sup>1</sup> Hydrological Sciences Laboratory, NASA Goddard Space Flight Center, 8800 Greenbelt Road, Greenbelt, Maryland 20771

<sup>2</sup> Universities Space Research Association/GESTAR, 7178 Columbia Gateway Dr, Columbia, Maryland 21046

Corresponding author: Dalia Kirschbaum ([dalia.kirschbaum@nasa.gov](mailto:dalia.kirschbaum@nasa.gov))

## Key Points:

- A system has been developed to provide near real-time estimates of potential landslide activity in the tropics and middle latitudes
- Openly available remote sensing and landslide inventory data is a key foundation for developing, adapting and validating this system
- This open-source system is designed to improve understanding of the spatial and temporal distribution of landslide hazards

## Abstract

Determining the time, location, and severity of natural disaster impacts is fundamental to formulating mitigation strategies, appropriate and timely responses, and robust recovery plans. A Landslide Hazard Assessment for Situational Awareness (LHASA) model was developed to indicate potential landslide activity in near real-time. LHASA combines satellite-based precipitation estimates with a landslide susceptibility map derived from information on slope, geology, road networks, fault zones, and forest loss. Precipitation data from the Global Precipitation Measurement (GPM) mission are used to identify rainfall conditions from the past seven days. When rainfall is considered to be extreme and susceptibility values are moderate to very high, a “nowcast” is issued to indicate the times and places where landslides are more probable. When LHASA nowcasts were evaluated with a Global Landslide Catalog, the probability of detection (POD) ranged from 8 to 60%, depending on the evaluation period, precipitation product used, and the size of the spatial and temporal window considered around each landslide point. Applications of the LHASA system are also discussed, including how LHASA is used to estimate long-term trends in potential landslide activity at a nearly global scale and how it can be used as a tool to support disaster risk assessment. LHASA is intended to provide situational awareness of landslide hazards in near real-time, providing a flexible, open source framework that can be adapted to other spatial and temporal scales based on data availability.

### 1 Introduction

Determining the time, location, and severity of natural disaster impacts is fundamental to formulating mitigation strategies, appropriate and timely responses, and robust recovery plans. For disasters that can affect broad areas, such as earthquakes or tropical cyclones, global networks of ground-based or satellite systems provide operational real-time monitoring. Globally focused earthquake systems, such as the Global Seismic Network (GSN, <https://www.iris.edu/hq/programs/gsn>), support a permanent digital system of state-of-the-art seismological and geophysical sensors connected by a telecommunications network. The International Seismological Centre (<http://www.isc.ac.uk>) provides the longest definitive summary of global seismicity leveraging ~130 seismic networks and data centers around the world. The USGS National Earthquake Information Center (NEIC, <http://earthquake.usgs.gov/contactus/golden/neic.php>) rapidly distributes information on the location and size of all significant earthquakes that occur worldwide. Information from these networks or centers is used by emergency response organizations, government agencies, and the general public to improve awareness of the affected areas, anticipated level of damage (e.g. the USGS PAGER system; <https://earthquake.usgs.gov/data/pager>), and aftershock information is also used by the seismologic research community.

Tropical cyclones are monitored by systems in space, including geostationary infrared satellites such as the NOAA Geostationary Satellite Server (GOES, <http://www.goes.noaa.gov>) series, microwave data from the Joint Polar Satellite System (JPSS, <http://www.jpss.noaa.gov>), Global Precipitation Measurement (GPM, <https://pmm.nasa.gov>) mission and its global constellation, and many others. These data are used by operational warning centers, such as the Joint Typhoon Warning Center, Naval Research Lab, and National Hurricane Center in the United States, and many other numerical weather prediction centers worldwide. The magnitude of other hazards, including fires, volcanoes, and floods, can be monitored by satellite or airborne

instruments in thermal, visible, and microwave frequencies. However, few efforts have approached landslide hazard monitoring or situational awareness at a consistent global scale.

Mass movements, including debris flows, landslides, mudflows, rockfalls, etc. (herein referred to as landslides) occur in nearly every country on earth, cause thousands of fatalities, and result in significant infrastructure impacts and disruption of livelihoods each year [Petley, 2011; Kirschbaum *et al.*, 2015b]. One challenge with in situ or remote monitoring of these events is that landslides can range in size from a few meters to several kilometers in length and span at least ten orders of magnitude in volume [Malamud *et al.*, 2004]. They occur over a broad range of lithologies, morphologies, hydrologic settings, land covers, and climatic zones and are triggered by intense or prolonged rainfall, seismic activity, rapid temperature changes, and anthropogenic activities such as mining, construction, improper drainage, land use change, and deforestation [Keefer, 1994; Larsen and Parks, 1997; Larsen and Roman, 2001; Glade, 2003; Guzzetti *et al.*, 2008]. Characterizing the location and timing of landslide events over broad areas is extremely challenging due to the wide range of atmospheric and subsurface conditions that can result in slope failure, as well as the imprecision in our knowledge of those conditions.

Landslide hazards have been monitored in many ways. Ground-based instrumentation for monitoring a single hillslope can identify the potential for slope movement [Malet *et al.*, 2002; Oppikofer *et al.*, 2009; Casagli *et al.*, 2010]. Operational landslide monitoring systems have been implemented at the country or city level primarily by utilizing ground-based precipitation radar or gauge networks. The Italian Civil Protection Department (<http://www.protezionecivile.gov.it>) uses radar data to make estimates of slope failures induced by rainfall that they turn into warnings and broadcast across the country. The Japan Meteorological Agency (<https://www.jma.go.jp/en/doshamesh/>) has a national system that is based on 60-minute cumulative rainfall and soil–water index thresholds derived from ground-based radar to support an early-warning system [Osanai *et al.*, 2010]. A national landslide early warning system is operated by the Norwegian Water Resources and Energy Directorate to monitor and forecast hydrometeorological conditions that could potentially trigger landslides [Devoli *et al.*, 2015]. Rio de Janeiro, Brazil has developed a system called Alerta Rio (<http://alertario.rio.rj.gov.br/>) that uses rainfall thresholds at different gauge locations across the city and a landslide susceptibility map. The Mayor’s office then decides whether to issue alerts or evacuation orders. Other examples of local monitoring sites, such as those managed by the U.S. Geological Survey (<https://landslides.usgs.gov/monitoring/>), have been established for specific landslides or high risk areas and may use rain gauges, slope movement sensors and soil moisture probes for monitoring.

The approach to dynamic landslide hazard assessment largely depends on the needs of the community, geographic area, and spatial scales considered. Rainfall is the most widespread and frequent trigger of landslides around the world [Petley *et al.*, 2005]; therefore, effectively characterizing the triggering patterns associated with rainfall is of high priority. However, establishing thresholds is complicated by the large variability in rainfall based on seasonality, geography, and climatology [Guzzetti *et al.*, 2008], as well as the relationships between rainfall and snow, antecedent soil moisture, and other natural and anthropogenic processes. Understanding the susceptibility of the terrain to landslide initiation is also important, but the accuracy and availability of this information varies from region to region. Different monitoring systems are also built to resolve particular types of landslides. Rapid, shallow debris flows

triggered by a short, high intensity rainstorm differ from deep-seated landslides caused by above average seasonal precipitation. Another challenge is the transformation of information from early warning systems into decisions about when and where to evacuate or mobilize response.

Satellite, airborne, and ground-based remote sensing data have served an important role in advancing the assessment of landslide hazards over local to regional scales. Local area studies have used visible imagery [e.g. *Hervas et al.*, 2003; *Nichol and Wong*, 2005; *Stumpf and Kerle*, 2011], light detection and ranging (LIDAR) [e.g. *Schulz*, 2007; *Jaboyedoff et al.*, 2012; *Crawford*, 2014], and interferometric synthetic aperture radar (SAR) data [e.g. *Hilley et al.*, 2004; *Calabro et al.*, 2010; *Handwerger et al.*, 2013] to delineate landslide scars following a triggering event (e.g. major storm or earthquake) or to map the prior landslide distribution. These data have also been used to derive digital elevation models (DEM), which can be computed from airborne or satellite sources such as the Shuttle Radar Topography Mission (SRTM), Advanced Spaceborne Thermal Emission and Reflection Radiometer (ASTER), or LIDAR instruments that characterize the terrain morphology [e.g. *Nichol et al.*, 2006; *Tarolli et al.*, 2012]. Further information from platforms such as Landsat can be used to define surface cover classes and evaluate how land cover is changing over time [e.g. *Hansen et al.*, 2013]. Lastly, satellite-based information on the meteorological conditions contributing to slope failures can be gleaned from precipitation data such as NASA's precipitation measurement missions (<https://pmm.nasa.gov>): Tropical Rainfall Measuring Mission (TRMM) and GPM, among other precipitation products.

Only a few research efforts to date have synthesized some of these data sources and triggering or conditioning variables to assess landslide hazard over regional to global scales. The first quasi-global near real-time, satellite-based system was proposed by [*Hong et al.*, 2006]. It combined TRMM rainfall data with a global landslide susceptibility map [*Hong et al.*, 2007]. Other research at the global scale has characterized landslide hazard statically [*Nadim et al.*, 2006] or retrospectively over time [*Farahmand and AghaKouchak*, 2013], but does not provide information routinely or in near real-time. Regional efforts have highlighted the use of remote sensing sources for dynamic characterization of landslide hazards or early warning [e.g. *Rossi et al.*, 2012; *Kirschbaum et al.*, 2015a; *Liao et al.*, 2012], but these are typically parameterized locally with landslide or rainfall gauge data that are not widely or publicly available, limiting its application over other regions. The increasing openness of data and advancement of geospatial tools including geographic information systems, commercial and free image-processing software, high-level programming languages as well as cloud computing and machine learning has increased the opportunities to better utilize Earth observation data for landslide mapping and hazard assessment. However, there remain significant opportunities to fuse multiple remotely sensed sources to characterize landslide hazards in a way that is easily accessible, rapidly disseminated, and applicable for improved situational awareness.

This work presents a Landslide Hazard Assessment for Situational Awareness (LHASA) model that provides information on rainfall-triggered landslide potential, defined as the times and places where landslides are more probable relative to other locations. This information is available in near real-time utilizing publicly available remotely sensed data and other globally available products. The model is intended to characterize landslides triggered by rainfall, with a focus on rapid movements within steeper terrain. LHASA generates landslide "nowcasts" from high quality, low-latency precipitation data from the Integrated Multi-satellitE Retrievals for GPM (IMERG) [*Huffman et al.*, 2015] and terrain information from a global landslide

susceptibility map [Stanley and Kirschbaum, 2017]. The motivation for this study is to leverage some of the new or publicly available datasets derived from remote sensing and other sources to approximate the potential conditions that result in slope failures. Due to the availability of low-latency rainfall information, the model can represent these conditions in near real-time, providing a relative, nearly global perspective that can be used to further refine study areas or conduct additional assessment of landslide impacts at the local scale. This paper outlines the methodology behind LHASA, the calibration and validation data, the procedure used to assess system performance, and the data access portal where this information can be extracted. This work also highlights applications of LHASA, including estimation of long-term trends in potential landslide activity at a nearly global scale and use as a tool to support disaster hazard assessment. The paper concludes with how this information should be utilized and discusses uncertainties, limitations, and paths forward for this work.

## 2. Data

The data used to develop and validate LHASA were nearly all from publicly available sources with near-global coverage, providing the opportunity for others to replicate or improve this system without significant cost barriers. Table 1 highlights the data used to develop LHASA.

Data Type	Data Set	Resolution	Explanatory Variable	Extent	Source and Details
<b>Elevation</b>	Viewfinder Panoramas Digital Elevation Data	3 arcseconds	Slope	84° N - 72° S	[de Ferranti, 2014] derived from 3-arc-second SRTM DEM and several other sources; <a href="http://viewfinderpanoramas.org/">http://viewfinderpanoramas.org/</a>
<b>Faults and Geologic Regions</b>	Geological Map of the World, 3rd edition	1:50,000,000	Distance to fault zones	Global	[Bouysse, 2010]; <a href="http://ccgm.org">http://ccgm.org</a>
			Lithologic classification	Global	[Bouysse, 2010]; <a href="http://ccgm.org">http://ccgm.org</a>
<b>Roads</b>	OpenStreetMap	Variable	Presence of roads	Global	[OpenStreetMap Contributors, 2015] Data represents OSM on June 4 <sup>th</sup> , 2015
<b>Forest Cover</b>	Global Forest Change 2000–2013	30 meters	Forest Loss	80° N – 60° S	[Hansen et al., 2013]
<b>Rainfall</b>	Integrated Multi-satellitE Retrievals for GPM (IMERG)	0.1° x 0.1°, 30-minute	Rainfall accumulation	60° N – S	[Huffman et al., 2015]; <a href="https://pmm.nasa.gov/data-access/downloads/gpm">https://pmm.nasa.gov/data-access/downloads/gpm</a>
	TRMM Multisatellite Precipitation Analysis (TMPA)	0.25° x 0.25°, 3-hour	Rainfall accumulation	50° N – S	[Huffman et al., 2010]; <a href="https://pmm.nasa.gov/data-access/downloads/trmm">https://pmm.nasa.gov/data-access/downloads/trmm</a>
<b>Landslide Catalog</b>	Global Landslide Catalog	Variable	Landslide reports	Global	[Kirschbaum et al., 2010, 2015b]; <a href="https://data.nasa.gov/Earth-Science/Global-Landslide-Catalog/h9d8-neg4">https://data.nasa.gov/Earth-Science/Global-Landslide-Catalog/h9d8-neg4</a>

**Table 1.** Description of explanatory variables used to develop and validate LHASA, including variables to develop the global susceptibility map (rows 1-4), rainfall triggering (rows 5-6) and landslide inventory (row 7).

## 2.1 Susceptibility Map

A static representation of the terrain's potential for a slope failure is represented by a global landslide susceptibility map that includes five explanatory variables: slope, distance to fault zones, geology, presence of roads, and forest loss (Table 1). These five variables were selected after an analysis of nine different susceptibility studies conducted at regional to global scales as well as analysis of the availability, quality, and performance of the variables. The methodology for computing the susceptibility map is described in detail by Stanley and Kirschbaum [2017]. Slope was computed from a global DEM produced by *de Ferranti*, [2014], who merged SRTM 3-arcsecond data with additional topographic maps to improve the characterization of elevation in complex terrain where SRTM is known to have issues with data voids. Distance to fault zones and geological classification was derived from the Geological Map of the World, 3rd edition, which was purchased for €50. A revised 3<sup>rd</sup> edition was made available in 2014 at 1:35,000,000 scale but was not available when this study was done. The geological classification was computed following the methodology outlined in [*Nadim et al.*, 2006]. Distance to major faults (both active and inactive) was calculated to create a proxy for tectonic activity, which can destabilize soil, rock and debris on slopes and increase potential for future slope failures [*Marc et al.*, 2015]. The road network from OpenStreetMap® [*OpenStreetMap Contributors*, 2015] was simplified to the presence or absence of a road within each 1-km pixel of the susceptibility map in order to represent the more frequent occurrence of landslides near roads. Finally, a variable for forest loss was extracted from [*Hansen et al.*, 2013], which provides a binary output of forest loss calculated from global Landsat maps between 2000-2013. The 30-m pixels were aggregated to 1 km and are used to represent forest cover change due to many causes, including timber harvesting, fire, and storms that may have destabilizing impacts on the surface and subsurface. The resulting map is currently a static representation of landslide susceptibility; however, the variables of roads, forest loss, and slope have the potential to be updated with additional versions of the data or with new datasets when available. This is beyond the scope of the current study.

A fuzzy overlay model [*Bonham-Carter*, 1994] was used to combine the five explanatory variables into a global susceptibility map at a 1-km resolution. First, geology, roads, forest loss, and faults were assigned values between zero and one through functions that describe membership in a fuzzy set. Next, these fuzzy membership values were merged with a fuzzy gamma operator, which is a function that combines explanatory variables into a single fuzzy membership value, for each pixel. In order to ensure that no flat ground was classified as highly susceptible, this output was combined with slope through the fuzzy product operator, which emphasizes the lesser of two inputs. The susceptibility values output by the fuzzy overlay model were then classified into five categories: Very Low, Low, Moderate, High, and Very High. These categories are not equally sized; Very Low represented approximately half of the world's land surface, while Very High represented approximately 3%. The methods for overlay and binning are described in [*Stanley and Kirschbaum*, 2017]. The susceptibility map is intended to provide a relative picture of susceptibility that can be comparable globally and is most relevant for rapid slope failures occurring in moderate to high relief. This map may be less informative for landslides occurring on gradual terrain (e.g. large, slow moving failures in quick clays) or in areas that have been extensively modified by anthropogenic activity (e.g. mining, construction).

The global susceptibility map is shown in Figure 1a and is available for download at <https://pmm.nasa.gov/applications/global-landslide-model>.

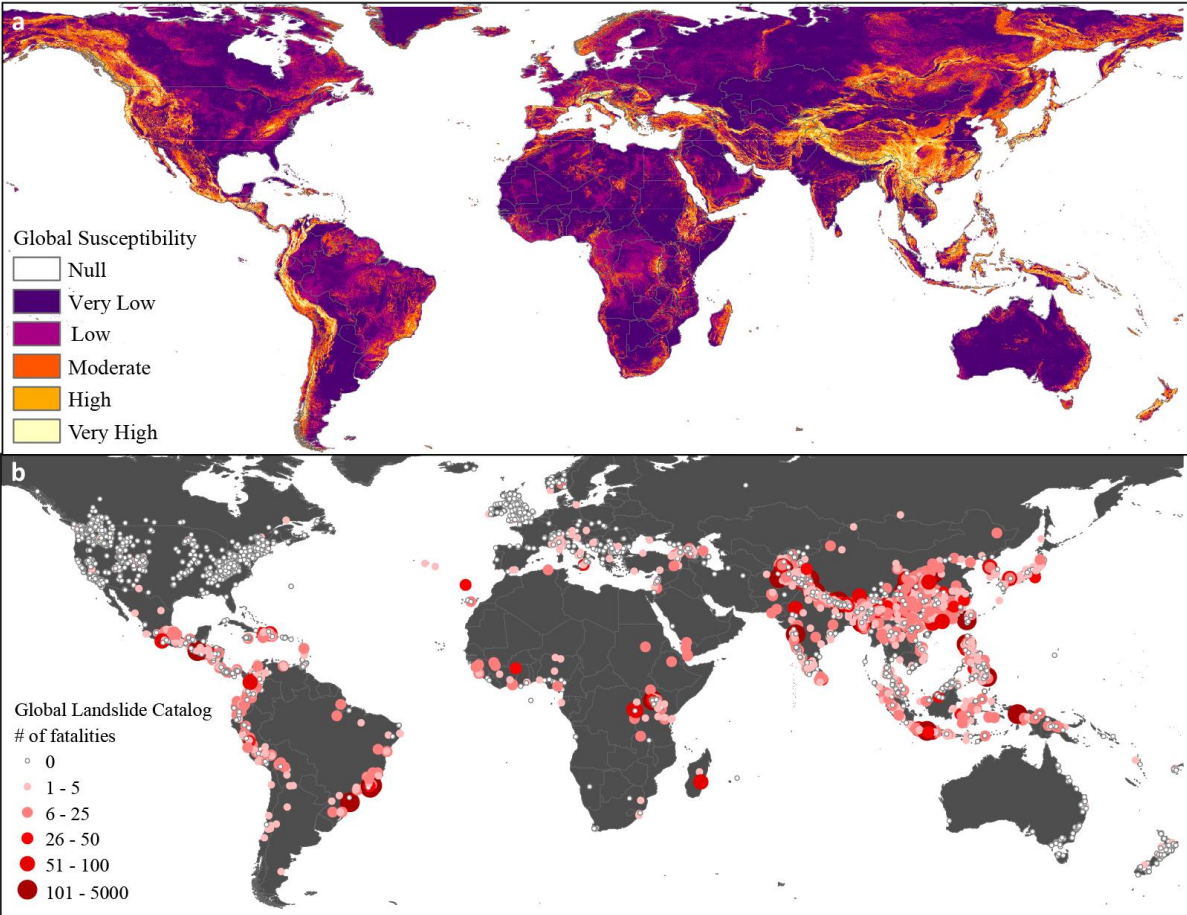


**Figure 1. a)** Global landslide susceptibility map computed using slope, geology, fault zones, road networks, and forest loss [Stanley and Kirschbaum, 2017]; **b)** Global Landslide Catalog (2007-2016) showing the distribution of landslide fatalities [Kirschbaum et al., 2015b].

## 2.2 Rainfall Data

NASA’s remotely sensed precipitation products provide the ability to estimate rainfall accumulation around the world in near real-time. The TRMM Multi-satellite Precipitation Analysis (TMPA) [Huffman et al., 2010] product provides rainfall information at a 0.25° pixel resolution from 50°N-S using the TRMM satellite’s passive and active microwave data, as well as other microwave radiometers, and infrared data to fill in gaps between overpasses. The TRMM satellite was launched in 1997 and provided observations of moderate to heavy precipitation in the tropics and subtropics until April 2015. The TMPA product continues to be produced through 2018 to ensure overlap with its successor products from GPM. The Integrated Multi-satellitE Retrievals for GPM (IMERG) [Huffman et al., 2015] has a pixel resolution of 0.1° and coverage from 60°N-S. The GPM Core Observatory satellite was launched in February 2014 and extends TRMM’s capabilities by providing broader coverage and estimates of both falling snow and light to heavy rainfall. LHASA takes advantage of the long TMPA near real-time

record, available from 2000 to the 2017, as well as the increased resolution and quality of the IMERG product. There are several different products provided for both TMPA and IMERG. For this analysis TMPA-RT (real-time) and the IMERG-Early (latency of 4 hours) and IMERG-Late (latency of 12-18 hours) are used. The methodology section outlines how the satellite-based rainfall products were used for estimation of potential landslide triggering.

There is a broad and diverse field of literature evaluating the reliability, robustness and quality of satellite-based precipitation estimates of TMPA, with emerging publications for IMERG analysis as well (see <https://pmm.nasa.gov/resources/gpm-publications>). Publications have evaluated and effectively utilized the TMPA product for hydrometeorological hazard applications across different spatial and temporal domains [Li *et al.*, 2009; Nikolopoulos *et al.*, 2013; Yaduvanshi *et al.*, 2015; Abdelkareem, 2017; Cloke *et al.*, 2017]. While a robust analysis of the product performance is outside the scope of this study, thorough documentation of each product is available at <https://pmm.nasa.gov/data-access/downloads>.

### 2.3 Landslide Inventories

One of the persistent challenges in developing a landslide model at a regional or global scale is the dearth of landslide inventory information with which to evaluate the outputs. A Global Landslide Catalog (GLC) has been developed for rainfall-triggered landslides reported by the media, online databases and other sources and provides data from 2007 to the present [Kirschbaum *et al.*, 2010, 2015b]. The publicly available database of over 9,500 events includes information on the location (latitude, longitude, and place name), date and time if available, impacts (fatalities, injuries), and a qualitative metric to account for landslide size (small to very large) and location confidence (known within a radius of kilometers). Distribution of the GLC from 2007-2016 is shown in Figure 1b. The landslide size and location confidence metrics are described in Kirschbaum *et al.* [2010, 2015a].

Due to its compilation methodology, there are many inherent uncertainties and biases that are described including: language (reports are almost exclusively obtained from reports written in English), geographic reporting (landslide is more likely to be reported proximate to population and infrastructure), inclusion of landslide impacts with other hazards such as floods or tropical cyclones, and regional reporting biases due to political instability, press restrictions, and other limitations. There are also biases inherent in the process of manually entering a landslide report, depending on the amount of information available within the source. There are no adjustments made to this catalog to account for regional or population biases and a quantitative or systematic review of these biases are outside the scope of this paper. Despite its limitations, the GLC is the largest global public inventory of landslides to our knowledge. The GLC was the primary dataset used to evaluate the LHASA model; however, many other regional inventories were used to calibrate and validate the global susceptibility map, which is detailed in [Stanley and Kirschbaum, 2017].

## 3 Methods

The methodology used to produce LHASA originated in studies of Central American landslide hazard [Kirschbaum *et al.*, 2015a]. This flexible framework combines static variables, such as slope and geology, with dynamic variables, such as recent precipitation, into a heuristic

decision tree model. In order to describe landslide hazard over a much larger and less homogeneous area than Central America, LHASA employs different thresholds for landslide susceptibility and rainfall triggering.

### 3.1 Antecedent Rainfall Index

There have been many different treatments of how to represent the landslide-triggering rainfall threshold. Caine [1980] provided the first global representation of landslide triggering by proposing an intensity-duration threshold, indicating a value of rainfall accumulation for a given storm duration that was more likely to trigger a landslide. Subsequent efforts have summarized these thresholds in various ways, including normalized daily rainfall [Terlien, 1998], normalized rainfall intensity [Cannon, 1988], critical volume of water [Keefer *et al.*, 1987], intensity-duration [Hong *et al.*, 2006; Guzzetti *et al.*, 2007], and compilations of multiple intensity-duration thresholds calculated by region [Guzzetti *et al.*, 2008], among many others. More recently, researchers have automated the process of determining landslide-triggering precipitation [Segoni *et al.*, 2014; Vessia *et al.*, 2014], or combined recent and antecedent rainfall [Scheevel *et al.*, 2017].

One of the challenges with applying a uniform global rainfall intensity-duration threshold is the extreme variability in precipitation regimes and climate zones around the world. To this point, 50 mm of rainfall in a 1-day period in a tropical region with frequent, intense afternoon thunderstorms may have a lower likelihood of landsliding compared to a more arid region where the same rainfall event could represent a 100-year recurrence interval storm. To account for the differences between sites, this work leverages the 16-year record of continuous rainfall from TMPA and calculates an Antecedent Rainfall Index (ARI) similar to models previously proposed [Crozier, 1999; Glade *et al.*, 2000]. The ARI computes a weighted average of the most recent 7 days of rainfall, including the current date. Then,

$$(1) \quad ARI = \frac{\sum_{t=0}^6 p_t w_t}{\sum_{t=0}^6 w_t}$$

where  $t$  = the number of days before the present,  $p_t$  = the precipitation at time  $t$ , and  $w_t = (t+1)^{-2}$ . The weighting exponent of -2 and the length of the 7-day window were calibrated at the locations of 949 landslides from the years 2007-2013. Several combinations of weighting coefficients and spatial windows were tested, and the best predictor of landslides was selected on the basis of distance to perfect classification [Cepeda *et al.*, 2010].

The ARI was computed at a daily time step retrospectively from 2000-2014. Then an extreme ARI threshold, defined as the 95<sup>th</sup> percentile of the historical ARI values, was assigned for each TMPA pixel. TMPA data was used for this purpose, because the short record currently available for IMERG is likely to bias results due to recent events, such as the 2015-16 El Niño. Due to differences in sensor, algorithm, and resolution between TMPA and IMERG, it was necessary to transform the ARI thresholds developed using TMPA-RT to be applicable with IMERG. Therefore, a pixel-based quantile mapping technique was applied and is described in depth in [Stanley *et al.*, 2017]. In quantile mapping, a value from one data product is used to look up the value of the second product at the same quantile (Figure 2a). For this application, specific percentiles for daily TMPA and IMERG rainfall were computed for each pixel. TMPA values

were resampled to a  $0.1^\circ$  grid by the nearest neighbor method. Due to the spatial extent of TMPA between  $50^\circ$  north and south, the output of LHASA is restricted to these boundaries. The IMERG algorithm will be reprocessed in 2018 to provide a continuous dataset with its current spatiotemporal resolution from 2000-present. At that point, the ARI values will be recomputed from the extended IMERG record and there will no longer be a need for the quantile mapping between TMPA and IMERG. In some very arid areas, the 95th percentile ARI is still low. In order to avoid erroneous predictions in desert regions, a conservative minimum ARI threshold of 6.6 mm (equivalent to 10 mm precipitation per day) was adopted. The ARI values used for LHASA at the 95<sup>th</sup> percentile are shown in Figure 2b.

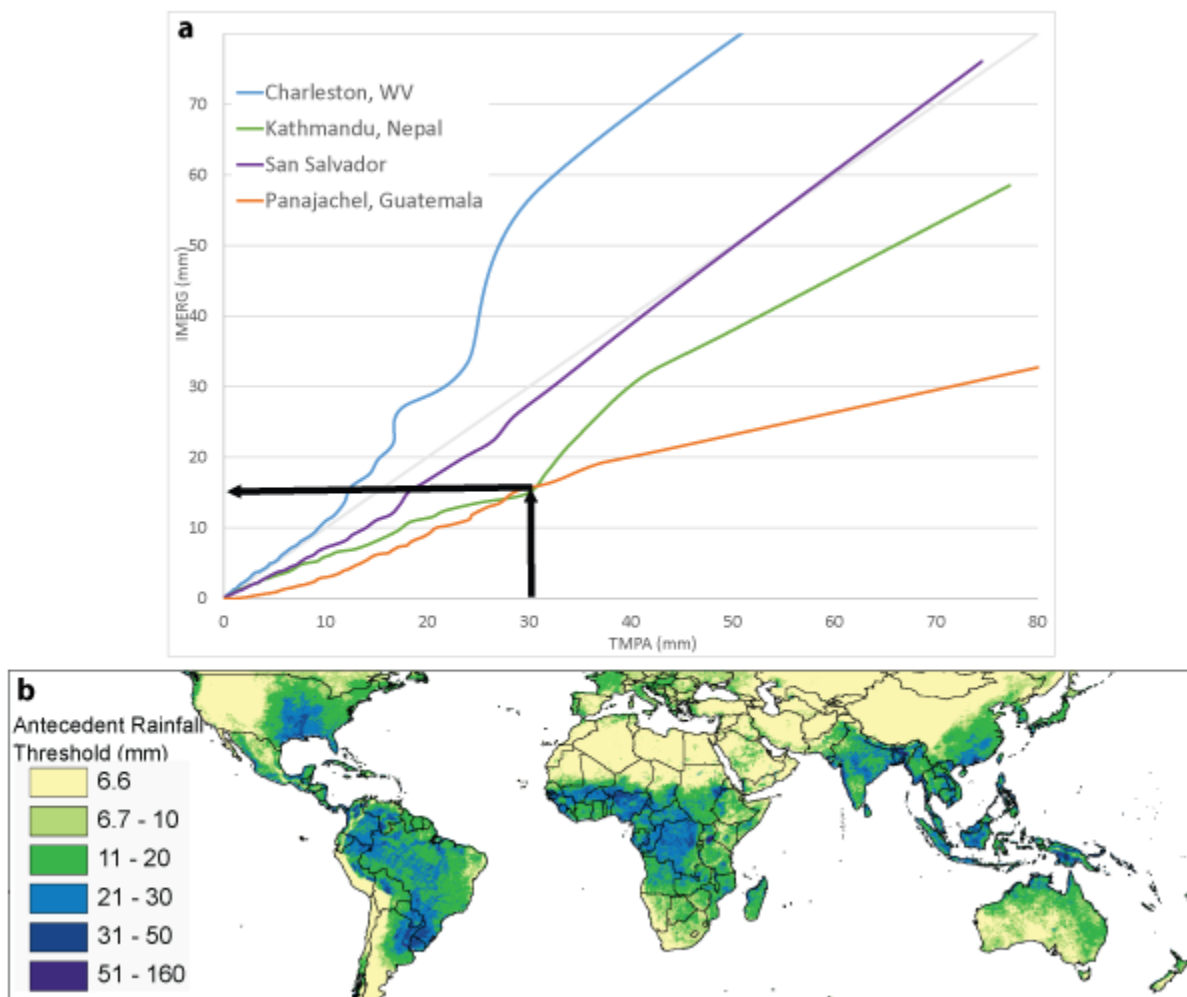


**Figure 2. a)** Quantile mapping procedure for several locations: Charleston, West Virginia (blue), Kathmandu, Nepal (Green), San Salvador, El Salvador (Purple), and Panajachel, Guatemala (Orange). The black arrows show how the quantile mapping procedure would work for

Kathmandu where the TMPA 95<sup>th</sup> percentile value of 30 mm would be remapped to 15 mm for IMERG. Plot **b)** shows ARI values used in LHASA following the quantile mapping application.

### 3.2 Decision Tree Framework

The LHASA decision tree framework is described in Figure 3. It combines a 7-day rainfall index with a landslide susceptibility map.

Step 1: The ARI is computed every three hours at each 0.1° IMERG pixel. IMERG-Early data is used to represent the past 24 hours of rainfall, then the IMERG-Late represents the rainfall accumulations for the previous 6 days. This is done to take advantage of the improved accuracy of the IMERG-Late product. The ARI total is compared against the pixel's 95th percentile threshold. If the accumulated rainfall is below this value, no nowcast is issued but if the ARI exceeds the threshold then the susceptibility map is consulted.

Step 2: If the susceptibility is considered low to very low, no nowcast is issued. If susceptibility is moderate to high, a moderate-hazard nowcast is issued; finally if the susceptibility is very high, then a high-hazard nowcast is issued. The nowcast results are updated every 30 minutes.

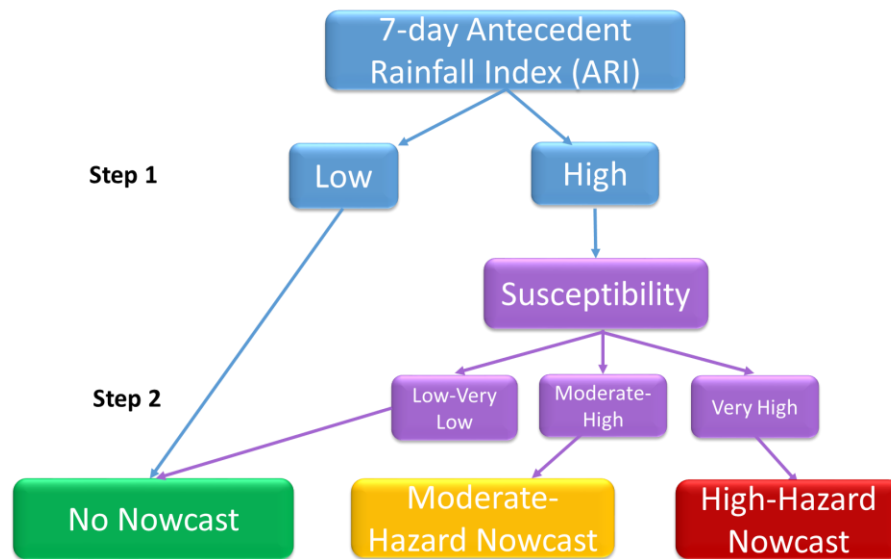


**Figure 3.** LHASA decision tree structure for generating near real-time landslide hazard nowcasts. In this structure, an ARI is calculated using IMERG-Early and IMERG-Late data every 30 minutes for the previous 7 days. A global susceptibility map [Stanley and Kirschbaum, 2017b] is considered and nowcasts are issued if the susceptibility values are moderate to high (moderate-hazard nowcast), or very high (high-hazard nowcast).

### 3.3 Data Access

Figure 4 provides an example of LHASA output for both high and moderate nowcasts for 9 October 2016. This figure shows the distribution and number of LHASA nowcasts generated for a single time slice and highlights the landslide reports from the GLC that occurred on the same date as LHASA output. LHASA is currently running as a prototype in near real-time at

<https://pmm.nasa.gov/precip-apps>. The model takes about 3.6 minutes to compute LHASA nowcasts running on a single core every 30 minutes. The model is being run on an Intel Xeon E5-2690 2.6 Ghz single-threaded system at the NASA Precipitation Processing System. Nowcasts can be queried by region and can be exported as either a GEOTIFF, geoJSON, ArcJSON, or Shapefile. These data are stored for the previous 60 days and then deleted; however, a research version of this dataset is archived for model validation and testing. For easy access via the web, nowcast results are vectorized with Potrace [Selinger, 2017]. These data can be obtained via an Applications Programmer Interface (API). Documentation on how to use this API along with sample code is available at <https://pmmpublisher.pps.eosdis.nasa.gov/docs>. Additional products are available through the same interface, including IMERG-Early 30-minute, 3-hour, and 1-day accumulations; IMERG-Late 1-, 3-, and 7-day accumulations; and a global flood nowcast [Wu *et al.*, 2014]. The LHASA code has been made fully open source on GitHub (<https://github.com/vightel/ojo-bot/tree/master/python>) and is written in Python 2.7. This code is also available in R upon request.

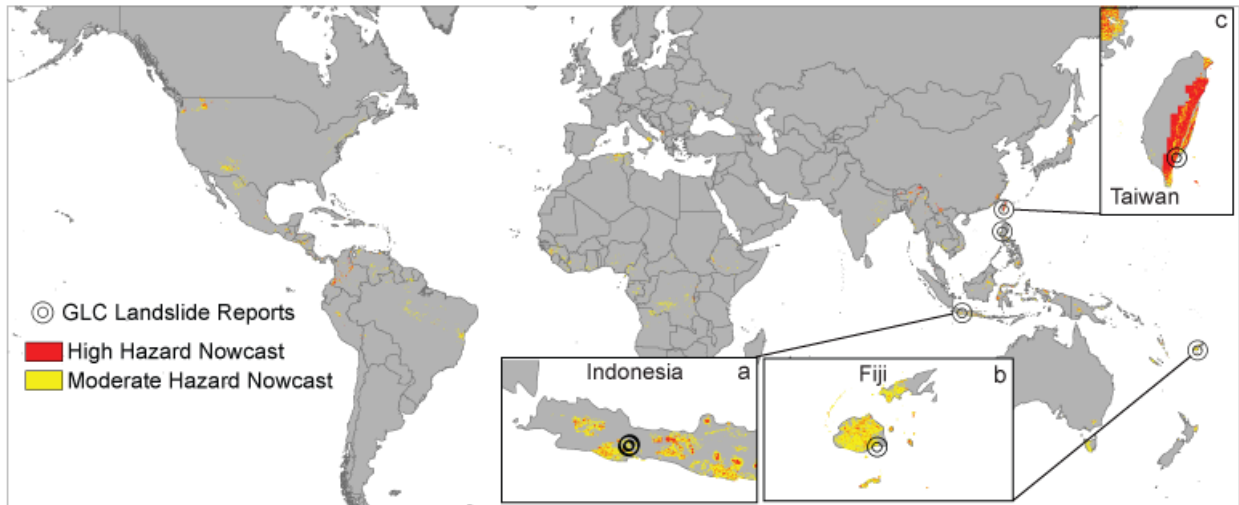


**Figure 4.** Map of LHASA output for moderate (yellow) and high (red) nowcasts for 9 October 2016. Inset maps provide a zoom into some regions with larger areas of potential landslide activity and indicate landslides that occurred on the same day including a) Central Java, Indonesia, b) Fiji, and c) Taiwan.

### 3.4 Model validation

The LHASA model was run retrospectively using the TMPA-based ARI thresholds for 2001-2016, and for the IMERG period with the quantile-mapped IMERG values from March 25 2014 to October 2, 2017. Nowcast results were evaluated with the GLC. The true positive rate (TPR) was assessed by determining whether each of the 4,930 landslide events in the GLC was predicted by the high- or moderate-hazard nowcasts. These events were chosen by eliminating all landslide reports with a spatial accuracy worse than ten kilometers based on the GLC metric for “location confidence” provided in each report. Only reports with rainfall as the known trigger were included for validation purposes. The possibility of temporal errors in the reporting of events in the GLC was addressed by evaluating windows of varying temporal length (Table 2). The 1-day window evaluated whether a nowcast was issued on the exact date of a reported landslide. The 3-day window allowed for the possibility that time zone differences between

IMERG (UTC) and the landslide's location (locally variable) may exist by counting an event as a true positive if it was predicted on the day before, during, or after the reported date. All events with known times were adjusted to UTC dates, but the majority of reports in the GLC do not contain exact times. The 7-day window considered the possibility of errors in the original landslide report by counting an event as a true positive if the nowcast predicted a landslide at any point from 5 days before to one day after the reported date. The long-term false positive rate (FPR) was defined as the proportion of pixel-days for which a nowcast was issued, but no landslide was reported.

A landslide is more likely to be reported at the location of human impacts, which often exists in the landslide runout area rather than the initiation zone of the landslide. Therefore, model validation could be affected by the facts that potential initiation zones are the focus of the landslide nowcasts and that the susceptibility map may not capture these runout zones if the event runs out over a long distance. Due to the uncertainty in location of the GLC points, a spatial buffer was applied to determine the extent to which uncertainty in the report's latitude and longitude affected the validation results. The variable spatial buffer was applied to each GLC point by creating a circle with a radius based on the reported location accuracy for each GLC entry. Any nowcast within the spatial buffer was determined an accurate detection. Results for the exact GLC locations and with application of a spatial buffer are summarized in Table 2. Results are also shown for a separate landslide database provided by *Petley et al.*, [2007] in Nepal (Table 3).

Because LHASA relies exclusively on IMERG for determining landslide triggering, the nowcasts are unlikely to characterize landslide activity caused by factors other than rainfall, such as earthquakes, snowmelt, extreme temperature, anthropogenic activities, or events with unknown triggers. In addition, as summarized in *Kirschbaum et al.*, [2010, 2015b] and Section 2.3, the GLC does not provide a comprehensive catalog of all rainfall-triggered landslides worldwide and may have errors related to existing reports.

## 4 Results

LHASA has two categories to approximate potential rainfall-triggered landslide activity: moderate and high nowcasts. The highest hazard level (red) is designed to highlight locations where landslides may be more likely to occur due to factors such as steep slopes, deforestation, seismicity, and road building. The moderate-hazard level represents a compromise between the needs for specificity and comprehensiveness. This area is depicted in yellow. Approximately 1% of the land surface (or 5% of the susceptible land surface) between 50° North and 50° South is identified as moderately hazardous on any given day.

### 4.1 Model Evaluation

LHASA was run retrospectively using TMPA data from January 1, 2007 to December 31, 2016, and again using IMERG data from March 25, 2014 through October 2, 2017. LHASA outputs were compared to the GLC over 3 temporal windows. The TPR and FPR for the moderate and high-hazard nowcasts are summarized in Table 2. TPR increases as temporal windows grow longer. The overall FPR for the moderate hazard nowcast was 1%, although this rate differed by location, with a rate of over 5% in a few pixels, and a rate of 0% in most

locations. The overall FPR for the high hazard nowcast was 0.2%, with a rate of over 5% in a few pixels. Similar effects can be seen after the application of spatial buffers. The accuracy of many reports used for this analysis is better than 1 kilometer, but most points are only accurate within a radius of 5 or 10 kilometers. Thus, the doubling of TPR for the high-hazard model after application of spatial buffers is not surprising.

		TPR (%)			FPR (%)	Number of validation points
	Time period and rainfall product evaluated	1-day	3-day	7-day		
Moderate Hazard	2007-16 (TMPA)	27	39	47	1	4930
	2014-17 (IMERG)	24	35	40	1	2100
High Hazard	2007-16 (TMPA)	10	14	18	0.2	4930
	2014-17 (IMERG)	8	14	16	0.2	2100
After application of spatial buffer						
Moderate Hazard	2007-16 (TMPA)	34	49	60	NA	4930
	2014-17 (IMERG)	28	41	46	NA	2100
High Hazard	2007-16 (TMPA)	24	34	41	NA	4930
	2014-17 (IMERG)	18	27	31	NA	2100

**Table 2.** True Positive Rates (TPR) and False Positive Rates (FPR) within varying temporal windows for both the Moderate and High Hazard nowcasts. LHASA was evaluated using TMPA data from 2007-2016 and IMERG data from March 25 2014 to October 2, 2017. The bottom four rows of the table provide results when a spatial buffer was applied to each GLC point according to the reported location accuracy, rather than at the reported latitude and longitude of the GLC point. FPR is calculated for the world as a whole; therefore, the pixels within each spatial buffer are not comparable to the overall rate and are shown as “NA”.

Model outputs were also compared to an independent database of fatal landslides in Nepal compiled by Petley et al. [2007], which includes 384 landslides from 2007-2016 (Table 3). Results over this region show improved performance relative to the global analysis, which is likely due several factors. First, this database is generally found to have a higher spatial and temporal precision relative to the GLC of the reports due to the compilation methodology and restriction of the database to only fatal events. When the spatial accuracy of each landslide report is taken into account, the results between the global and Nepal analysis are similar (Table 2). Second, this analysis is conducted over a region with moderate to very high susceptibility and frequent high rainfall values, resulting in more frequent landslide nowcasts.

		TPR (%)			FPR (%)	Number of validation points
	Time period and rainfall product evaluated	1-day	3-day	7-day		
Moderate Hazard	2007-16 (TMPA)	32	47	58	3	384
	2014-16 (IMERG)	40	50	60	3	82
High Hazard	2007-16 (TMPA)	22	33	40	1	384
	2014-16 (IMERG)	26	30	39	2	82

**Table 3.** True positive Rates (TPR) and False Positive Rates (FPR) within varying temporal windows for Petley’s Nepal database [Petley *et al.*, 2007]. False positive rates are higher in Nepal due to the prevalence of susceptible terrain in this region.

#### 4.2 Patterns of landslide hazard across space and time

In addition to situational awareness, LHASA can be used to delineate areas where unreported landslides are probable. Figure 5 shows the annual frequency of moderate and high hazard nowcasts globally from 2001-2016 using TMPA. Figure 6a compares the distribution of moderate hazard nowcasts to the GLC from 2007-2016. Figure 6 also highlights several regions around the world where the GLC does not have many events reported, including b) the southern Andes, c) the East African Rift Zone, and d) Turkey and Iran.

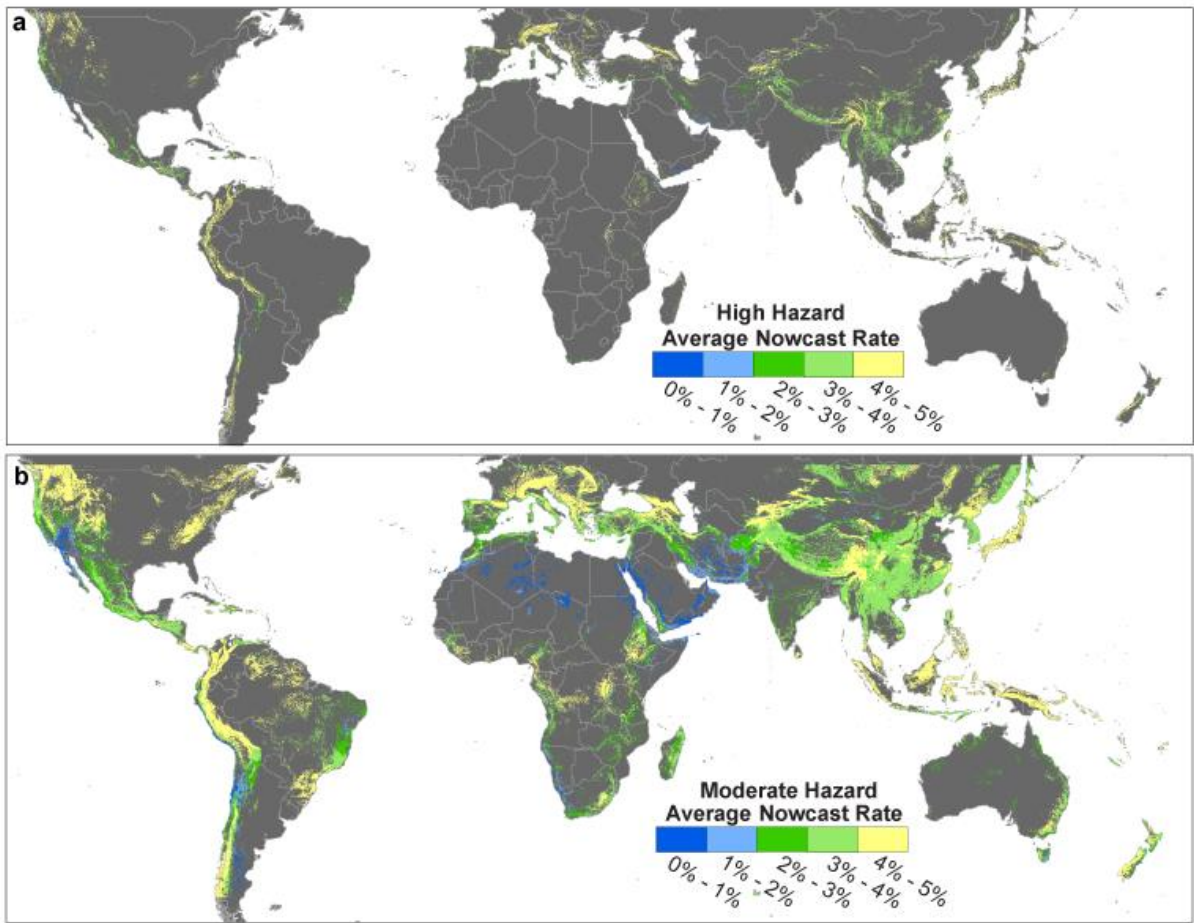


**Figure 5.** Annually averaged percentage of days (or nowcast rate) that each pixel has either **a)** high-hazard or **b)** moderate-hazard nowcasts from 2001-2016 using the TMPA precipitation data. Results highlight areas with a higher likelihood of landslide potential on average across the

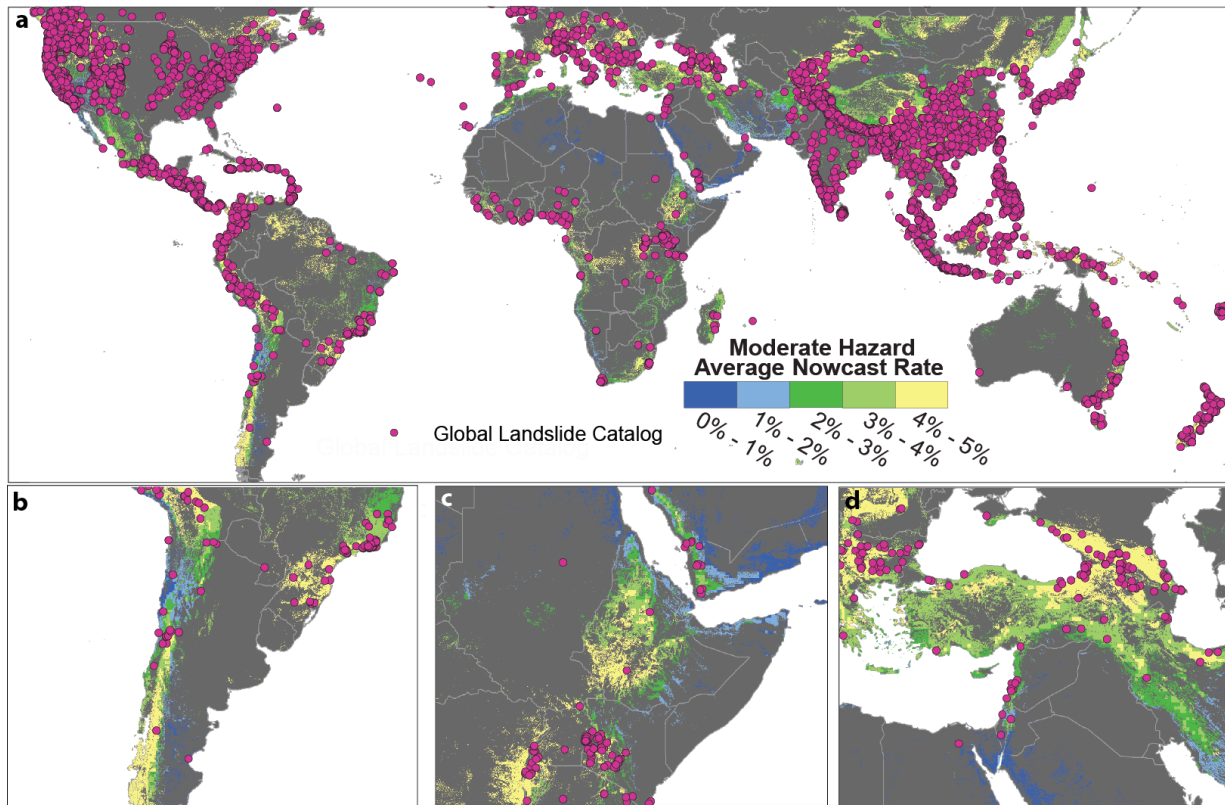


**Figure 6.** The figure overlays annually averaged moderate-hazard nowcasts with the GLC from 2000-2016 to highlight areas where landslide potential may be expected but there is a dearth of GLC reports. Specifically graph shows (a) global distribution, (b) the Southern Andes, (c) East African Rift Zone, and (d) Turkey and Iran. Existing catalogs like the GLC may be missing key areas that have the potential to experience landslide activity.

Retrospective analysis using the LHASA model characterizes the “landslide season” by region, suggesting periods of the year with high levels of potential landslide activity. Figure 7 shows the average monthly distribution of high and moderate hazard nowcasts globally for 2001-2016 along with the total number of events by month in the GLC for 2007-2016. Results show a peak in nowcasts and GLC reports in July and August, likely corresponding to the Asian monsoon and tropical cyclone seasons in the Atlantic and Pacific. A secondary peak is identified in December and January. Figures 8 further illustrates this seasonal reversal of average moderate hazard nowcast rates, showing results for Peru in January (a) and July (b) and for East and Southern Asia for the same months (c-d). Results show clear spatial and seasonal differences in the moderate nowcast rate, or percentage of the time a nowcast is generated, for both regions, averaged from 2001 – 2016. There is an interesting latitudinal gradient in Figure 8c and d over the Philippines, where the northern portion of the country has a peak in moderate nowcasts in July while the southern region peaks in January. This likely corresponds to the movement of the Intertropical Convergence Zone. Figure 9 shows the average monthly patterns in moderate and high nowcasts for Peru and Taiwan along with the total GLC landslides reported for 2007 to 2016. The LHASA nowcasts for the two regions highlight clear seasonal signals in potential landslide activity, which are somewhat resolved by the GLC points but with less consistency.

Seasonal projections of landslide hazard, exposure or risk could be made for any other region of interest within the tropics or mid-latitudes.

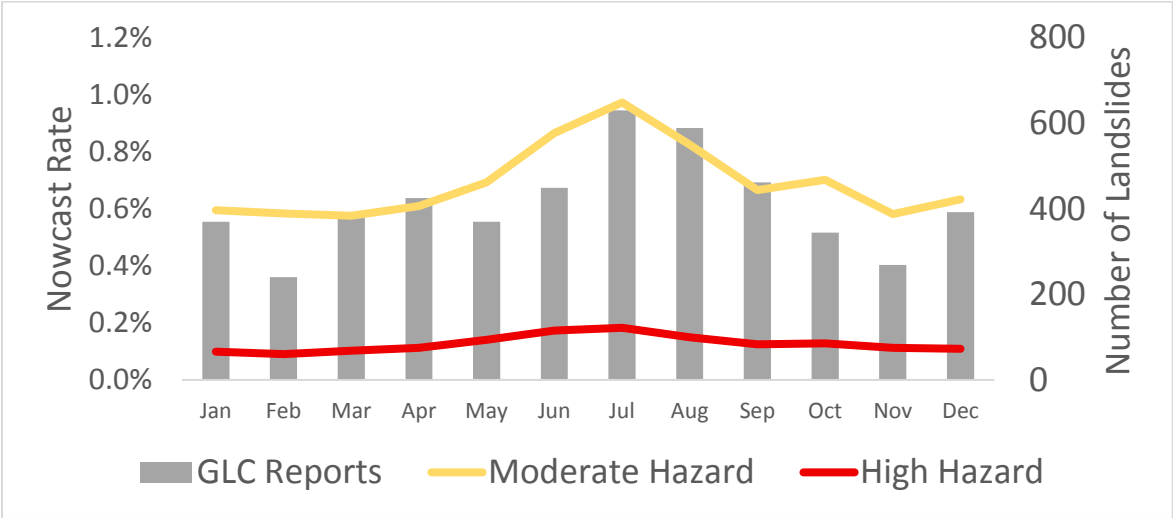


**Figure 7.** The average monthly rate of moderate and high hazard nowcasts for 2001 to 2016, with the total number of landslides reported from 2007 to 2016. Both landslides and nowcasts peak in July and August, with a second peak in December and January.

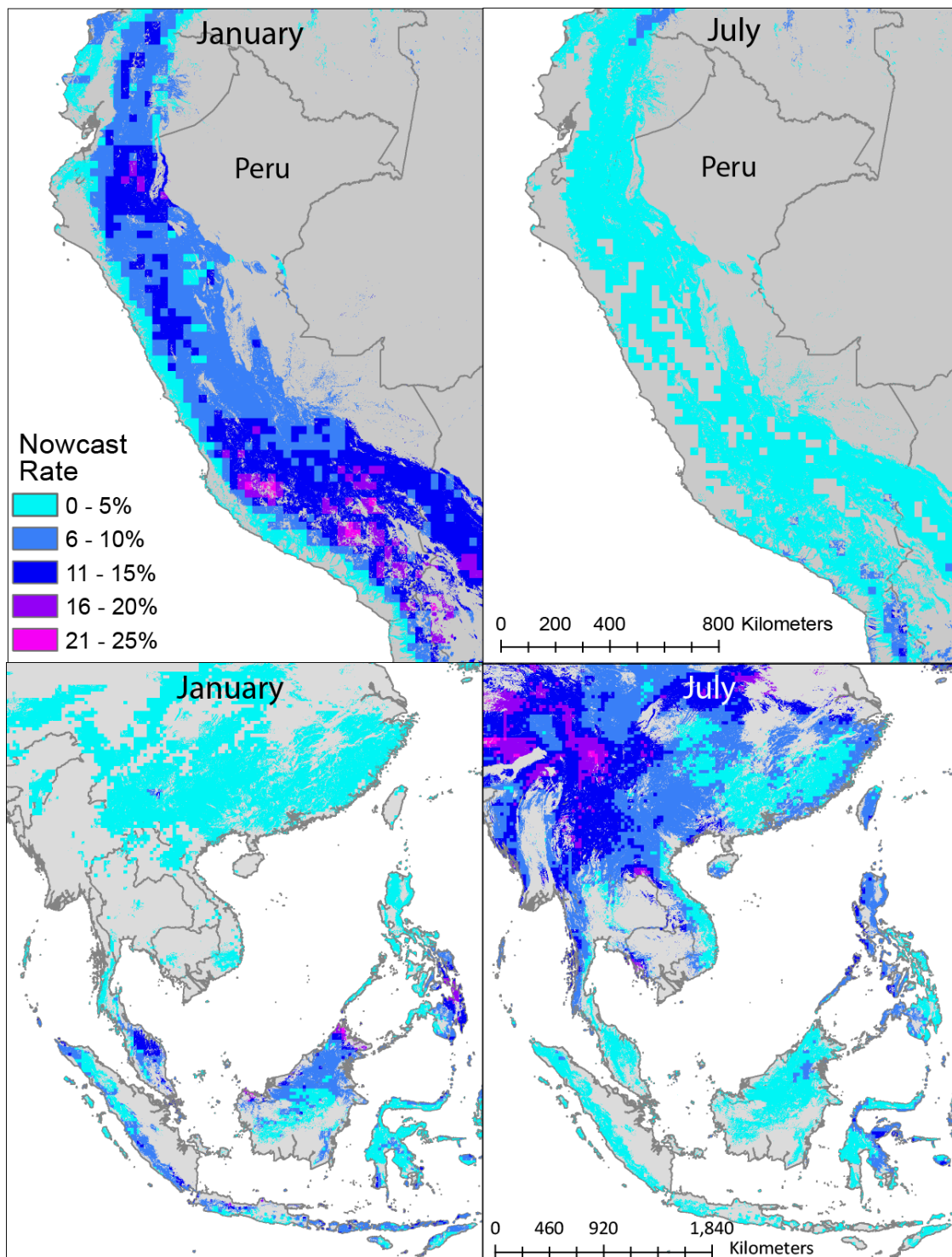


**Figure 8.** Seasonal patterns in moderate hazard nowcasts for January (left) and July (right) for Peru (top) and East and Southern Asia (bottom).

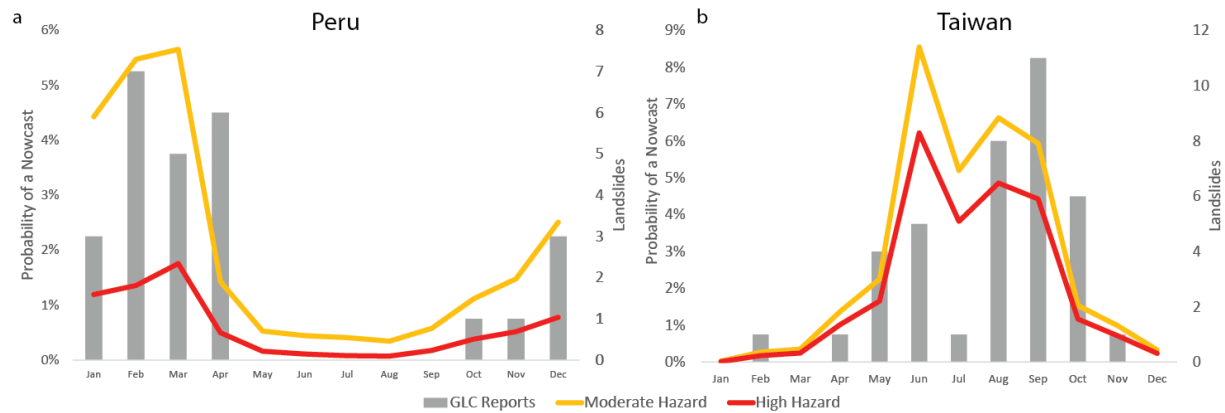


**Figure 9.** Average monthly moderate (yellow) and high (red) nowcasts for a) Peru and b) Taiwan for 2001-2016, with the total number of landslides reported in the areas from 2007 to 2016.

## 5 Discussion

### 5.1 Modeling challenges and future work

LHASA can be used to characterize potential landslide activity in a consistent way across the globe in near real-time. Validation results shown in Tables 2 and 3 highlight performance of the model at the global scale and within Nepal using a separate inventory provided by Petley et al. [2007], respectively. Results suggest that variability in the spatial and temporal accuracy of the GLC may have a significant impact on the apparent performance of LHASA. Considering a broader spatiotemporal window surrounding each reported event can increase the overall probability of detection by over 10%. This could be explained in 3 ways: 1) the longer the window is the more likely unrelated rainfall events will be detected; 2) many landslide reports may be inaccurate (due to time zone issues or other sources of error) or the date of landslide initiation may fall within the longer window but not on the reported date; or 3) sometimes there may be a gap in time after a rainfall event and landslide initiation [Helmstetter and Garambois, 2010; Huang et al., 2012]. While both FPR rates are relatively low, this number would be more robust if there were a global database of “non-landslide” points. Given the absence of such a database at even local or regional scales, the acceptability of the FPR value depends upon the specific application of the landslide nowcast, which is discussed through several end user examples below. Other performance metrics may be more suitable to evaluate this model; however, the authors felt that a more standard confusion matrix approach would allow for clear and concise performance metrics as well as comparison with other studies.

While promising as a system, there are many inherent limitations of the LHASA model as a result of the geographic scope and variables considered. Of foremost importance is the need for improved, spatially consistent landslide inventories to better parameterize and validate LHASA at regional and global scales. Efforts are underway to develop a new citizen science platform “Landslide Reporter” that will enable users to share landslide event or inventory information, search existing data, and export the full catalog. This system will enable data sharing across the globe in an effort to increase the availability, completeness, and accuracy of landslide information for studies such as this. A future version of the LHASA and Landslide

Reporter systems may also enable citizen scientists to help validate the landslide nowcasts for rapid feedback and validation of the near real-time products.

A second challenge of the existing LHASA model is the reliance on a long data record to establish LHASA's triggering threshold. TMPA data provides a consistent record from 2000-2016; however, with the launch of GPM in 2014 and the decommissioning of the TRMM satellite in April, 2015, a quantile mapping procedure was needed to map thresholds from TMPA to IMERG. As discussed above, the IMERG dataset will ultimately be reprocessed back through the TRMM area (tentatively from 2000 to present), which will provide one continuous record from which to calculate new ARI thresholds. The LHASA ARI thresholds will be updated once the new IMERG data is released.

A third limitation of the system is its inability to resolve landslides occurring at higher latitudes where snow, frozen precipitation, or freeze-thaw processes may significantly impact landslide occurrence. The TMPA product is only available up to 50°N-S and is designed to resolve moderate to heavy rainfall. As such, there are shortcomings of the current precipitation dataset due to its limitation in resolving light rain and frozen precipitation at higher latitudes. While IMERG has higher sensitivity to these precipitation processes, the record is currently too short for use. As a result of the thresholds selected and precipitation product used, the model is better at resolving landslides that occur on steeper slopes with rapid (less than 7-day) rainfall triggers compared to other landslide types like shallow quick clays that can occur on more gradual surfaces or rock falls which may be triggered by a complex set of variables.

A fourth challenge is the determination of the ARI, which uses the exponent -2 that was calibrated from available data. However, the speed at which soil moisture declines will not be consistent across the globe or for different soil horizons. The first step to improving this would be to use a satellite or satellite assimilated model data product for antecedent soil moisture, such as Level 4 products estimated from SMAP [Reichle *et al.*, 2016]. However, one challenge is that satellite-based soil moisture products tend to underperform in areas with dense vegetation or complex topography [Dorigo *et al.*, 2010]. Soil moisture algorithms incorporating modeled and satellite data are continuing to improve and future work may update this model to incorporate soil moisture. Another potential improvement could be to replace the ARI with a more physically based model that accounts for the hydromechanical dynamics of individual hillslopes, but limitations in accuracy of globally available datasets would make this very difficult.

Finally, the rainfall-triggering thresholds and susceptibility index values established for use in LHASA were designed based on previous work and available data to an extent, but may not be relevant for all types of applications. The tolerance for defining a null, moderate, or high nowcasts will differ by user and application. For example, many military or emergency response groups are looking for the "60% solution" (TPR>0.6), or for a set of ensembles that will allow them to rapidly diagnose the issue and generate their own action plans. This system is not intended for local planning or to inform detailed infrastructure projects due to its geographic scope and spatial resolution. LHASA is also *not* meant to be used as a warning or forecasting system. This is due to the model latency (4-5 hours from satellite acquisition of rainfall data) as well as the fact that different emergency responders, forecasters or even media will have different ways of representing landslide potential information to their end users.

## 579           5.2 Potential LHASA applications

580           While LHASA is still considered a prototype system, there are several examples of how  
 581 this system is either already being used or may be utilized in the future within a range of user  
 582 communities. The U.S. Army Geospatial Planning Cells (GPC) are responsible for databases of  
 583 geospatial information that support war-time and humanitarian operations around the world. One  
 584 example of collaborative work in this area is the El Nino extreme rains in Peru in 2015, where  
 585 there was widespread landsliding in many areas across the country. The global landslide  
 586 susceptibility map presented here and in Stanley and Kirschbaum [2017] was provided to the  
 587 Army Geospatial Center (AGC), who used the information to inform the U.S. Embassy in Peru  
 588 and Peruvian authorities about potential landslide activity. Using the map and satellite  
 589 precipitation information, they were able to identify several locations that had not previously  
 590 been considered. According to the Military Advisor to the Director of the Army Geospatial  
 591 Center, a landslide model running every 30 minutes routinely could “enable the staff for  
 592 Combatant Commanders to focus their planning efforts on the environmental risks associated  
 593 with humanitarian and disaster relief operations... and assist the staff in prioritizing equipment  
 594 and logistical resources to meet evolving environmental threats and target hazards to critical  
 595 resources” [Chief Jason Feser, *personal communication*, 2 October 2017]. Upon discussion with  
 596 this group, AGC also found significant value in having a simplified categorical metric for  
 597 potential activity (e.g. red, yellow, green) to enable the rapid prioritization of efforts. By  
 598 additionally providing the underlying information that goes into the model including the  
 599 susceptibility and rainfall (such as is available through the current portal), it enables the staff to  
 600 understand the objective risk and factor in operational risks. This information can be overlaid  
 601 with other underlying factors such as population or critical infrastructure to help inform and  
 602 dictate how resources or tactical equipment/personnel are distributed.

603  
 604           A second example of LHASA implementation points to its potential utility at a local  
 605 level. The advanced Rio de Janeiro warning system Alerta Rio (<http://alertario.rio.rj.gov.br/>)  
 606 brings together in situ information across the city to characterize potential risks and disseminate  
 607 warnings. The city is currently in the process of implementing the LHASA code within their  
 608 system to improve their real-time characterization of landslide potential across the city. Using  
 609 their own gauge network and precipitation forecasts made by their weather service as well as  
 610 their local susceptibility maps, the Mayor’s office in Rio is developing an application that can  
 611 run in real-time to improve the awareness of potential landslide affected areas and ultimately  
 612 provide watches and warnings to Rio’s population. The team implementing this system has been  
 613 consulting LHASA outputs for the city since early 2017 and has documented the accuracy of the  
 614 system within their area (both predicted landslides and accurate non-events).

615  
 616           A third user example highlights the opportunity for LHASA to inform situational  
 617 awareness within a multi-hazard framework. The Pacific Disaster Center (PDC;  
 618 <http://www.pdc.org/>) provides disaster situational awareness reports worldwide, working with  
 619 hundreds of countries to provide relevant data as well as value added products and analyses  
 620 during disaster events. Currently, the PDC ingests TRMM and GPM precipitation information  
 621 but has a limited amount of landslide data or models. They are interested in ingesting this  
 622 product due to its consistent methodology across the globe and finds several ways in which this

data could be applied. Therefore, the PDC found that “the annually averaged moderate- and high-hazard nowcasts...could be utilized to start national-level landslide mapping in places where no better information is available and/or to provide guide on where investments should be prioritized to obtain a better understanding of the landslide hazard” [Carlos Villacis and Chris Chiesa, PDC, *personal communication*, 26 September 2017]. LHASA may be further utilized if precipitation estimates were ingested from a forecast model to identify potential landslide occurrences in advance, enabling this system to be used as a tool for landslide warnings. PDC is also interested in how this model can address questions of landslide impacts by estimating potential landslide exposure within areas of strategic infrastructure, producing timely alerts that can aid in the implementation of mitigation options that could reduce losses.

Based on the above examples as well as other end user feedback, one of the highest priorities for future model development is to apply forecasted precipitation estimates to decrease the latency of potential landslide nowcasts. By incorporating global quantitative precipitation estimates such as those provided by the Global Forecast System (GFS; <https://www.ncdc.noaa.gov/data-access/model-data/model-datasets/global-forecast-system-gfs>) or Goddard Earth Observing System Model, Version 5 (GEOS-5; <https://gmao.gsfc.nasa.gov/systems/geos5/>), LHASA could provide a 24 or 48 hour outlook of future potential activity, making the outputs more applicable for rapid response. The LHASA model currently only considers rainfall triggers, but incorporating additional triggers including earthquakes, is a natural next step of this system. There is also the potential to partner with groups such as the USGS PAGER group to better account for antecedent moisture or landslide potential immediately following a major earthquake in order to better diagnose all of the potential conditions that may lead to landsliding. The current LHASA model only primarily considers the physical environment in terms of susceptibility, but evaluating the exposure of populations and infrastructure and ultimately extending this model to estimate risk are clear opportunities of this system.

## 5 Conclusions

The primary purpose of the landslide nowcast is to provide a broad perspective of rainfall-triggered landslide potential in near real-time. LHASA did not predict the majority of landslides in the GLC, which could be due to both errors in the GLC and the inability of a simple global model to describe a wide variety of hillslope processes. Despite its limitations, LHASA provides situational awareness and has several advantages over static maps or intensity-duration thresholds calibrated using a limited rainfall gauge network. First, LHASA is a straightforward decision tree framework that can be easily applied by a broad range of users with outputs that are simple and easily interpreted. The model runs quickly and exploits the availability of near real-time precipitation data to provide dynamic estimates of potential landslide activity. The components of LHASA, including the susceptibility map and its inputs, are publicly available. This allows people to replicate the methodology over their area of interest, or ultimately use the LHASA framework to input improved susceptibility and/or triggering information that is more relevant over their particular geographic area. By providing a consistent methodology across the globe, LHASA allows for the comparison between regions and supports further research into areas where landslide activity may be having a significant impact but is not well quantified. LHASA can also be used to look at how potential landslide activity varies seasonally, annually

or even across decadal scales at the global scale in a way that has not been fully possible up to this point.

Though the validation of the LHASA model remains challenging given the underreporting of landslides at the global scale, initial results suggest that the model demonstrates skill in resolving landslides reported in the GLC. Future work will focus on improving the rainfall-triggering threshold relationships, incorporating forecasted precipitation estimates into the model, and ultimately expanding the dynamic triggers within the model to account for other variables including seismic activity, and snowmelt. This type of system is designed specifically for organizations that require situational awareness of landslide hazards at regional to global scales, often in combination with other hazards and extreme events, so they may more effectively deliver aid, alert governments, and conduct further assessments of hazard impact. The ultimate goal of this work is that the LHASA model will continue to be improved as better landslide inventory information, surface or triggering variables, and more user feedback are available by our partners and the broader community.

## Acknowledgments

The authors gratefully acknowledge the end user groups that provided feedback on the utility of the LHASA model, including the Pacific Disaster Center, the Army Geospatial Center, and the Mayor's office in Rio de Janeiro, Brazil. The authors are also extremely thankful for the scientists and research staff that worked to populate the Global Landslide Catalog. Thank you also to David Petley for providing the additional landslide inventory data for Nepal used to evaluate the system, Matthew Lammers, who implemented and maintains the online version of this model and Pat Cappelaere who developed the preliminary Python version of LHASA and API for this code. This work was funded by the NASA Precipitation Measurement Mission. The data used to develop and implement LHASA are available through the following sites. The global landslide susceptibility map is available for download at: <https://pmm.nasa.gov/applications/global-landslide-model>. IMERG 30 minute precipitation data is available for download at <https://pmm.nasa.gov/data-access/downloads/gpm> or <https://pmm.nasa.gov/precip-apps>. LHASA nowcasts are available from the past 60 days at <https://pmm.nasa.gov/precip-apps>. The Global Landslide Catalog data is available at: <https://data.nasa.gov/Earth-Science/Global-Landslide-Catalog-Export/dd9e-wu2v>. The LHASA code is open source and available for download at <https://github.com/vightel/ojo-bot/tree/master/python>.

## References

- Abdelkareem, M. (2017), Targeting flash flood potential areas using remotely sensed data and GIS techniques, *Nat. Hazards*, 85(1), 19–37, doi:10.1007/s11069-016-2556-x.
- Bonham-Carter, G. (1994), *Geographic Information Systems for Geoscientists*, edited by D. F. Merriam, Pergamon, New York.

- Bouysse, P. (2010), *Geological Map of the World, 1:25,000,000 scale*.
- Caine, N. (1980), The Rainfall Intensity: Duration Control of Shallow Landslides and Debris Flows, *Geogr. Ann. Phys. Geogr.*, 62(1/2), 23–27.
- Calabro, M. D., D. A. Schmidt, and J. J. Roering (2010), An examination of seasonal deformation at the Portuguese Bend landslide, southern California, using radar interferometry, *J. Geophys. Res. Earth Surf.*, 115(F2), n/a-n/a, doi:10.1029/2009JF001314.
- Cannon, S. H. (1988), Regional rainfall-threshold conditions for abundant debris-flow activity, in *Landslides, floods, and marine effects of the storm of January 3–5, 1982, in the San Francisco Bay region, California*, edited by S. D. Ellen and G. F. Wieczorek, pp. 35–42, US Geological Survey.
- Casagli, N., F. Catani, C. Del Ventisette, and G. Luzi (2010), Monitoring, prediction, and early warning using ground-based radar interferometry, *Landslides*, 7(3), 291–301, doi:10.1007/s10346-010-0215-y.
- Cepeda, J., J. A. Chávez, and C. Cruz Martínez (2010), Procedure for the selection of runout model parameters from landslide back-analyses: application to the Metropolitan Area of San Salvador, El Salvador, *Landslides*, 7(2), 105–116, doi:10.1007/s10346-010-0197-9.
- Cloke, H. L., F. Pappenberger, P. J. Smith, and L. Victoria (2017), Early warnings of hazardous thunderstorms over Lake Victoria, *Early warnings of hazardous thunderstorms over Lake Victoria*, Contributors, O. (2015), OpenStreetMap®,
- Crawford, M. M. (2014), Inventory Mapping and Characterization of Landslides Using LiDAR : Kenton and Campbell Counties , Kentucky, in *Digital Mapping Techniques '11–12—Workshop Proceedings*, vol. 2014–1167, pp. 1–8, USGS Open-File Report.
- Crozier, M. J. (1999), Prediction of rainfall-triggered landslides: a test of the Antecedent Water Status Model, *Earth Surf. Process. Landforms*, 24, 825–833.
- Devoli, G., K. Ingeborg, S. Monica, O. Nils-Kristian, E. Ragnar, J. Erik, and C. Hervé (2015), Landslide Early Warning System and Web Tools for Real-Time Scenarios and for Distribution of Warning Messages in Norway, in *Engineering Geology for Society and Territory - Volume 2*, edited by G. Lollino, D. Giordan, G. B. Crosta, J. Corominas, R. Azzam, J. Wasowski, and N. Sciarra, pp. 625–629, Springer International Publishing, Cham.
- Dorigo, W. A., K. Scipal, R. M. Parinussa, Y. Y. Liu, W. Wagner, R. A. M. De Jeu, and V. Naeimi (2010), Error characterisation of global active and passive microwave soil moisture datasets, *Hydrol. Earth Syst. Sci.*, 14, 2605–2616, doi:10.5194/hess-14-2605-2010.
- Farahmand, A., and A. AghaKouchak (2013), A satellite-based global landslide model, *Nat.*

- Hazards Earth Syst. Sci.*, 13(5), 1259–1267, doi:10.5194/nhess-13-1259-2013.
- de Ferranti, J. (2014), Digital Elevation Data - with SRTM voids filled using accurate topographic mapping, *Viewfind. Panoramas*. Available from: <http://www.viewfinderpanoramas.org/dem3.html> (Accessed 17 November 2015)
- Glade, T. (2003), Landslide occurrence as a response to land use change: a review of evidence from New Zealand, *CATENA*, 51(3), 297–314, doi:[https://doi.org/10.1016/S0341-8162\(02\)00170-4](https://doi.org/10.1016/S0341-8162(02)00170-4).
- Glade, T., M. Crozier, and P. Smith (2000), Applying Probability Determination to Refine Landslide-triggering Rainfall Thresholds Using an Empirical “Antecedent Daily Rainfall Model,” *Pure Appl. Geophys.*, 157, 1059–1079.
- Guzzetti, F., S. Peruccacci, M. Rossi, and C. P. Stark (2007), Rainfall thresholds for the initiation of landslides in central and southern Europe, *Meteorol Atmos Phy*, 98(3–4), 239–267.
- Guzzetti, F., S. Peruccacci, M. Rossi, and C. P. Stark (2008), The rainfall intensity–duration control of shallow landslides and debris flows: an update, *Landslides*, 5, 3–17, doi:10.1007/s10346-007-0112-1.
- Handwerger, A. L., J. J. Roering, and D. A. Schmidt (2013), Controls on the seasonal deformation of slow-moving landslides, *Earth Planet. Sci. Lett.*, 377–378, 239–247, doi:<https://doi.org/10.1016/j.epsl.2013.06.047>.
- Hansen, M. C. et al. (2013), High-resolution global maps of 21st-century forest cover change., *Science*, 342(6160), 850–3, doi:10.1126/science.1244693.
- Helmstetter, A., and S. Garambois (2010), Seismic monitoring of Séchilienne rockslide (French Alps): Analysis of seismic signals and their correlation with rainfalls, *J. Geophys. Res. Earth Surf.*, 115(F3), doi:10.1029/2009JF001532.
- Hervas, J., J. I. Barredo, P. L. Rosin, A. Pasuto, F. Mantovani, and S. Silvano (2003), Monitoring landslides from optical remotely sensed imagery: the case history of Tessina landslide, Italy, *Geomorphology*, 54, 63–75, doi:10.1016/S0169-555X(03)00056-4.
- Hilley, G. E., R. Bürgmann, A. Ferretti, F. Novali, and F. Rocca (2004), Dynamics of Slow-Moving Landslides from Permanent Scatterer Analysis, *Science*, 304(5679), 1952 LP-1955.
- Hong, Y., R. Adler, and G. Huffman (2006), Evaluation of the potential of NASA multi-satellite precipitation analysis in global landslide hazard assessment, *Geophys. Res. Lett.*, 33(L22402), 1–5, doi:10.1029/2006GL028010.
- Hong, Y., R. Adler, and G. Huffman (2007), Use of satellite remote sensing data in the mapping of global landslide susceptibility, *Nat. Hazards*, 43(2), 245–256, doi:10.1007/s11069-006-9104-z.

- Huang, A.-B., J.-T. Lee, Y.-T. Ho, Y.-F. Chiu, and S.-Y. Cheng (2012), Stability monitoring of rainfall-induced deep landslides through pore pressure profile measurements, *Soils Found.*, 52(4), 737–747, doi:<https://doi.org/10.1016/j.sandf.2012.07.013>.
- Huffman, G. J., R. F. Adler, D. T. Bolvin, and E. J. Nelkin (2010), The TRMM Multi-satellite Precipitation Analysis (TMPA), in *Satellite Rainfall Applications for Surface Hydrology*, edited by F. Hossain and M. Gebremichael, pp. 3–22, Springer Verlag.
- Huffman, G. J., D. T. Bolvin, D. Braithwaite, K. Hsu, R. J. Joyce, and P. Xie (2015), *Algorithm Theoretical Basis Document (ATBD) for NASA Global Precipitation Measurement (GPM) Integrated Multi-satellitE Retrievals for GPM (IMERG)*.
- Jaboyedoff, M., T. Oppikofer, A. Abellán, M.-H. Derron, A. Loye, R. Metzger, and A. Pedrazzini (2012), Use of LIDAR in landslide investigations: a review, *Nat. Hazards*, 61, 5–28, doi:[10.1007/s11069-010-9634-2](https://doi.org/10.1007/s11069-010-9634-2).
- Keefer, D. K. (1994), The importance of earthquake-induced landslides to long-term slope erosion and slope-failure hazards in seismically active regions, *Geomorphology*, 10, 265–284.
- Keefer, D. K., R. C. Wilson, R. K. Mark, E. E. Brabb, W. M. Brown, S. D. Ellen, E. L. Harp, G. F. Wieczorek, C. S. Alger, and R. S. Zarkin (1987), Real-Time Landslide Warning during Heavy Rainfall, *Science* (80-. ), 238(4829), 921–925.
- Kirschbaum, D., T. Stanley, and Y. Zhou (2015a), Spatial and temporal analysis of a global landslide catalog, *Geomorphology*, 249, 4–15, doi:[10.1016/j.geomorph.2015.03.016](https://doi.org/10.1016/j.geomorph.2015.03.016).
- Kirschbaum, D. B., R. Adler, Y. Hong, S. Hill, and A. Lerner-Lam (2010), A global landslide catalog for hazard applications: method, results, and limitations, *Nat. Hazards*, 52(3), 561–575, doi:[10.1007/s11069-009-9401-4](https://doi.org/10.1007/s11069-009-9401-4).
- Kirschbaum, D. B., T. Stanley, and J. Simmons (2015b), A dynamic landslide hazard assessment system for Central America and Hispaniola, *Nat. Hazards Earth Syst. Sci.*, 15(10), 2257–2272, doi:[10.5194/nhess-15-2257-2015](https://doi.org/10.5194/nhess-15-2257-2015).
- Kirschbaum, D. B., T. Stanley, and J. Simmons (2015c), A dynamic landslide hazard assessment system for Central America and Hispaniola, *Nat. Hazards Earth Syst. Sci.*, 15(10), 2257–2272, doi:[10.5194/nhess-15-2257-2015](https://doi.org/10.5194/nhess-15-2257-2015).
- Kirschbaum, D. B., T. Stanley, and Y. Zhou (2015d), Spatial and Temporal Analysis of a Global Landslide Catalog, *Geomorphology*, doi:[10.1016/j.geomorph.2015.03.016](https://doi.org/10.1016/j.geomorph.2015.03.016).
- Larsen, M. C., and J. E. Parks (1997), How wide is a road? The association of roads and mass-wasting in a forested montane environment, *Earth Surf. Process. Landforms*, 22, 835–848.
- Larsen, M. C., and A. S. Roman (2001), Mass Wasting and Sediment Storage in a Small

- Montane Watershed: an Extreme Case of Anthropogenic Disturbance in the Humid Tropics, in *Geomorphic Processes and Riverine Habitat, Water Science and Application*, vol. 4, edited by J. M. Dorava, F. Fitzpatrick, B. B. Palcsak, and D. R. Montgomery, pp. 119–138, American Geophysical Union Monograph.
- Li, L., Y. Hong, J. Wang, R. F. Adler, F. S. Policelli, S. Habib, D. Irwn, T. Korme, and L. Okello (2009), Evaluation of the real-time TRMM-based multi-satellite precipitation analysis for an operational flood prediction system in Nzoia Basin, Lake Victoria, Africa, *Nat. Hazards*, 50(1), 109–123, doi:10.1007/s11069-008-9324-5.
- Liao, Z., Y. Hong, D. Kirschbaum, and C. Liu (2012), Assessment of shallow landslides from Hurricane Mitch in central America using a physically based model, *Environ. Earth Sci.*, 66(6), 1697–1705, doi:10.1007/s12665-011-0997-9.
- Malamud, B. D., D. L. Turcotte, F. Guzzetti, and P. Reichenbach (2004), Landslide inventories and their statistical properties, *Earth Surf. Process. Landforms*, 29, 687–711.
- Malet, J.-P., O. Maquaire, and E. Calais (2002), The use of Global Positioning System techniques for the continuous monitoring of landslides: application to the Super-Sauze earthflow (Alpes-de-Haute-Provence, France), *Geomorphology*, 43(1), 33–54, doi:https://doi.org/10.1016/S0169-555X(01)00098-8.
- Marc, O., N. Hovius, P. Meunier, T. Uchida, and S. Hayashi (2015), Transient changes of landslide rates after earthquakes, *Geology*, 43(10), G36961.1, doi:10.1130/G36961.1.
- Nadim, F., O. Kjekstad, P. Peduzzi, C. Herold, and C. Jaedicke (2006), Global landslide and avalanche hotspots, *Landslides*, 3, 159–173, doi:10.1007/s10346-006-0036-1.
- Nichol, J., and M. S. Wong (2005), Satellite remote sensing for detailed landslide inventories using change detection and image fusion, *Int. J. Remote Sens.*, 26(9), 1913–1926, doi:10.1080/01431160512331314047.
- Nichol, J. E., A. Shaker, and M.-S. Wong (2006), Application of high-resolution stereo satellite images to detailed landslide hazard assessment, *Geomorphology*, 76(1–2), 68–75, doi:https://doi.org/10.1016/j.geomorph.2005.10.001.
- Nikolopoulos, E. I., E. N. Anagnostou, and M. Borga (2013), Using High-Resolution Satellite Rainfall Products to Simulate a Major Flash Flood Event in Northern Italy, *J. Hydrometeorol.*, 14(1), 171–185, doi:10.1175/JHM-D-12-09.1.
- Oppikofer, T., M. Jaboyedoff, L. Blikra, M. Derron, and R. Metzger (2009), Characterization and monitoring of the Aknes rockslide using terrestrial laser scanning, *Nat. Hazards Earth Syst. Sci.*, 9, 1003–1019.
- Osanai, N., T. Shimizu, K. Kuramoto, S. Kojima, and T. Noro (2010), Japanese early-warning

- for debris flows and slope failures using rainfall indices with Radial Basis Function Network, *Landslides*, 7(3), 325–338, doi:10.1007/s10346-010-0229-5.
- Petley, D. N. (2011), Global deaths from landslides in 2010 (updated to include a comparison with previous years), *Landslide Blog*. Available from: <http://blogs.agu.org/landslideblog/>
- Petley, D. N., S. A. Dunning, and N. J. Rosser (2005), The analysis of global landslide risk through the creation of a database of worldwide landslide fatalities, in *Landslide Risk Management*, edited by O. Hungr, R. Fell, R. Counture, and E. Ebergardt, pp. 367–374, Balkema, Amsterdam.
- Petley, D. N., G. J. Hearn, A. Hart, N. J. Rosser, S. A. Dunning, K. Owen, and W. A. Mitchell (2007), Trends in landslide occurrence in Nepal, *Nat. Hazards*, 43, 23–44, doi:10.1007/s11069-006-9100-3.
- Reichle, R., G. De Lannoy, R. D. Koster, W. T. Crow, and J. S. Kimball (2016), *SMAP L4 9 km EASE-Grid Surface and Root Zone Soil Moisture Geophysical Data, Version 2.*, Boulder, Colorado USA.
- Rossi, M., D. Kirschbaum, S. Luciani, A. C. Mondini, F. Guzzetti, C. Nazionale, M. Alta, P. Università, and G. Space (2012), TRMM satellite rainfall estimates for landslide early warning in Italy : preliminary results, in *Remote Sensing of the Atmosphere, Clouds, and Precipitation IV*, vol. 8523, edited by T. Hayasaka, K. Nakamura, and E. Im, pp. 10–16, Proceedings of SPIE.
- Scheeval, C. R., R. L. Baum, B. B. Mirus, and J. B. Smith (2017), Precipitation Thresholds for Landslide Occurrence Near Seattle, Mukilteo, and Everett, Washington, *USGS Open File Rep. 2017-1039*, doi.org/10.3133/ofr20171039. doi.org/10.3133/ofr20171039.
- Schulz, W. H. (2007), Landslide susceptibility revealed by LIDAR imagery and historical records, Seattle, Washington, *Eng. Geol.*, 89(1–2), 67–87, doi:<https://doi.org/10.1016/j.enggeo.2006.09.019>.
- Segoni, S., G. Rossi, A. Rosi, F. Catani (2014), Landslides triggered by rainfall: A semi-automated procedure to define consistent intensity–duration thresholds, *Computers & Geosciences*, 63, 123–131, doi.org/10.1016/j.cageo.2013.10.009.
- Selinger, P. (2017), Potrace: Transforming bitmaps into vector graphics, *GNU General Public License*. Available from: <http://potrace.sourceforge.net/> (Accessed 20 October 2017)
- Stanley, T., and D. B. Kirschbaum (2017a), A heuristic approach to global landslide susceptibility mapping, *Nat. Hazards*.
- Stanley, T., and D. B. Kirschbaum (2017b), A heuristic approach to global landslide susceptibility mapping, *Nat. Hazards*, 87(1), 145–164, doi:10.1007/s11069-017-2757-y.

876 Stanley, T., D. B. Kirschbaum, G. J. Huffman, and R. F. Adler (2017), Approximating long-term  
877 statistics early in the Global Precipitation Measurement era, *Earth Interact.*, 21(3), 1–10,  
878 doi:10.1175/EI-D-16-0025.1.

879 Stumpf, A., and N. Kerle (2011), Combining Random Forests and object-oriented analysis for  
880 landslide mapping from very high resolution imagery, *Procedia Environ. Sci.*, 3, 123–129,  
881 doi:http://dx.doi.org/10.1016/j.proenv.2011.02.022.

882 Tarolli, P., G. Sofia, and G. Dalla Fontana (2012), Geomorphic features extraction from high-  
883 resolution topography: landslide crowns and bank erosion, *Nat. Hazards*, 61(1), 65–83,  
884 doi:10.1007/s11069-010-9695-2.

885 Terlien, M. T. J. (1998), The determination of statistical and deterministic hydrological  
886 landslide-triggering thresholds, *Environ. Geol.*, 35(2–3), 124–130.

887 Vessia, G., M. Parise, M. T. Brunetti, S. Peruccacci, M. Rossi, C. Vennari, and F. Guzzetti  
888 (2014), Automated reconstruction of rainfall events responsible for shallow landslides. *Nat.*  
889 *Hazards Earth Syst. Sci.*, 14, 2399–2408, doi:10.5194/nhess-14-2399-2014.

890 Wu, H., R. F. Adler, Y. Tian, G. J. Huffman, H. Li, and J. Wang (2014), Real-time global flood  
891 estimation using satellite-based precipitation and a coupled land surface and routing model,  
892 *Water Resour. Res.*, 2693–2717, doi:10.1002/2013WR014710.Received.

893 Yaduvanshi, A., P. K. Srivastava, and A. C. Pandey (2015), Integrating TRMM and MODIS  
894 satellite with socio-economic vulnerability for monitoring drought risk over a tropical  
895 region of India, *Phys. Chem. Earth, Parts A/B/C*, 83(Supplement C), 14–27,  
896 doi:https://doi.org/10.1016/j.pce.2015.01.006.